IEEE Access
Multidisciplinary | Rapid Review | Open Access Journal

SPECIAL SECTION ON MICROWAVE (X- AND S-BAND) MARINE RADARS FOR OCEAN SENSING

Received February 10, 2018, accepted March 20, 2018, date of publication March 30, 2018, date of current version April 23, 2018.

Digital Object Identifier 10.1109/ACCESS.2018.2821564

The Effect of Radar Ocean Surface Sampling on Wave Spectrum Estimation Using X-Band Marine Radar

AL-ABBASS AL-HABASHNEH, (Student Member, IEEE), CECILIA MOLONEY, (Member, IEEE), ERIC W. GILL, (Senior Member, IEEE), AND WEIMIN HUANG, (Senior Member, IEEE)

Department of Electrical and Computer Engineering, Memorial University of Newfoundland, St. John's, NL A1B 3X5, Canada

Corresponding author: Al-Abbass Al-Habashneh (alabbassa@mun.ca)

The work of E. W. Gill was supported in part by the Natural Sciences and Engineering Research Council of Canada Discovery under Grant 238263-2010 and Grant RGPIN-2015-05289 and in part by the Atlantic Innovation Fund Award to Memorial University.

ABSTRACT In this paper, the effect of the ocean surface sampling process on the ocean wave spectral estimation using the Cartesian Fourier transform (CFT) method on *X*-band marine radar data is investigated. Our analysis shows that the ocean surface sampling process involves a spatial averaging process that might be described as a 2-D low pass filter. Furthermore, a filter referred to as the inverse sampling averaging filter (ISAF) is proposed to be integrated with the CFT method in order to mitigate the effect of the sampling process. For validation, the CFT-with-ISAF method as well as the CFT-without-ISAF method were used to estimate ocean wave spectra and sea state parameters from *X*-band marine radar field data. The estimates from both methods were compared to ground truth estimates generated using TRIAXYS wave buoy data. The results show that the ISAF improves the CFT method in estimating ocean wave spectra. The recorded accuracy improvements in estimating the non-directional wave spectrum, the peak wave period, the mean wave period, the zero-crossing wave period, and the peak wave direction were 11%, 12%, 21%, 17%, and 34%, respectively. The performances of significant wave height estimation using the ISAF method and the standard CFT method were validated against ground truth estimates and found to be comparable.

INDEX TERMS Remote sensing, *X*-band marine radar, ocean wave spectral estimation, modulation transfer function.

I. INTRODUCTION

The ocean surface imaging process using X-band marine radars includes several non-linear mechanisms. These mechanisms affect the ocean wave spectra estimates obtained by the Cartesian Fourier Transform (CFT) method [1]–[3]. Figure 1 gives a general illustration of the radar imaging process of producing the radar output (or B-scan), shown in the upper right panel of Figure 1, as a product of the sampled ocean surface in polar coordinates, the shadowing, and tilt modulation, shown in the lower left, lower middle, and lower right panels of Figure 1, respectively. Shadowing occurs when higher waves block the radar signal from reaching lower waves and, hence, effectively hiding them [2]. Tilt modulation can be described as the dependency of the returned radar signal on incident angle, whereby a radar signal with a small incident angle is expected to have a stronger return. Among the radar imaging mechanisms, shadowing and tilt modulation have been considered to have the most effect in ocean wave spectral estimation using the CFT method. Due to the non-linearity and complexity of the shadowing and tilt modulation processes, their contributions to the estimated ocean wave spectra are not completely understood. Several studies have addressed shadowing and tilt modulation and proposed empirical models to mitigate their effects on the estimates of ocean wave spectra [2], [4]–[8]. On the other hand, the effect of ocean surface sampling has not been addressed in the literature. Rather, the sampling of the ocean surface by X-band marine radars is treated as a standard sampling in which the return scatter from different samples is recorded as the return scatter from the centre of those samples. However, what actually happens when the radar signal reflects from the ocean surface reveals that this assumption is not accurate. The reflected radar signal from a certain sample is collected from the entire area of the sample, which

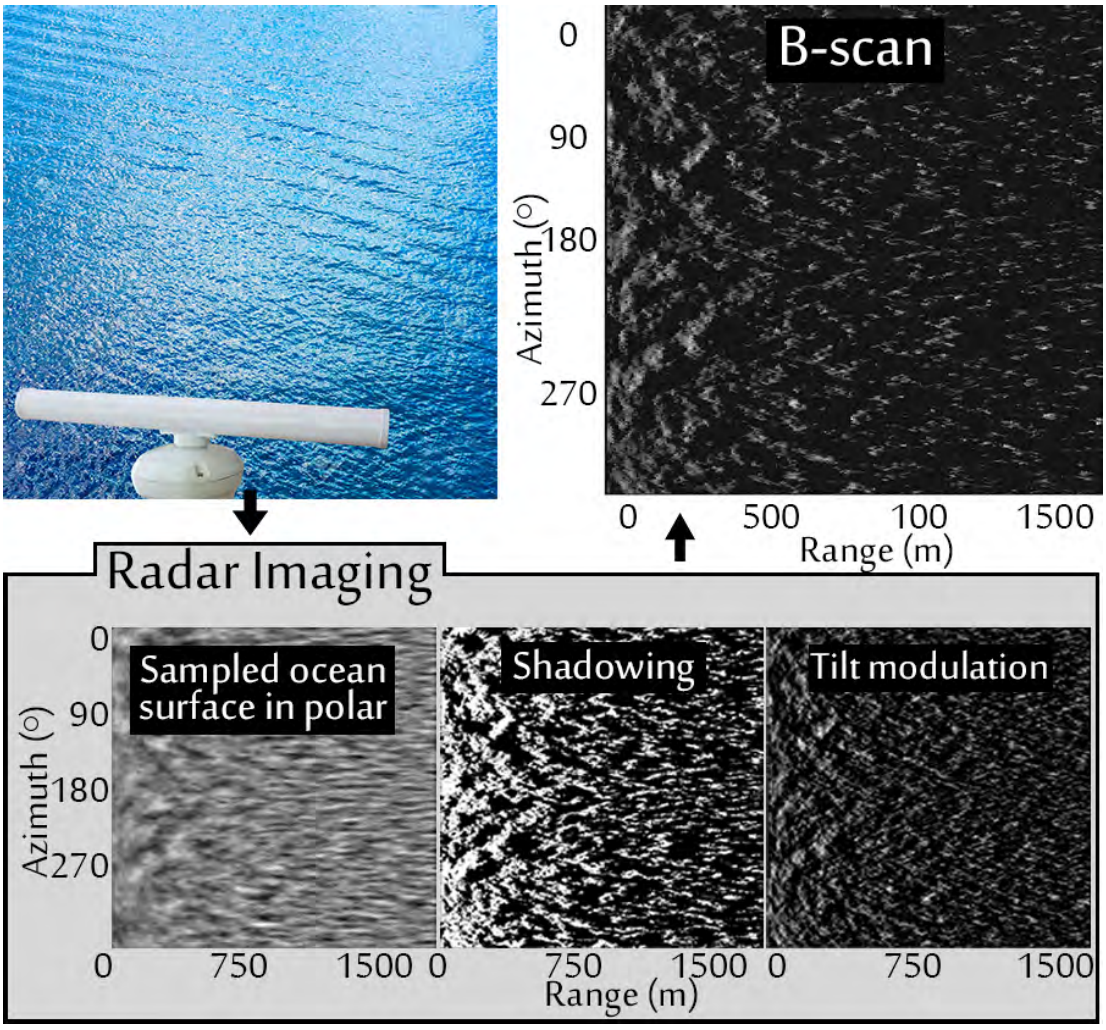

FIGURE 1. Illustration of the radar imaging process.

is determined by the radar parameters, and not only from its centre. This implies that the radar sampling process of the ocean surface involves an accumulating or averaging process that might affect the estimates of the ocean wave spectra. It must be noted that radars of different types, such as X-band and S-band, or different operation modes, such as short-pulse and mid-pulse [9], might have different spatial resolution. Therefore, the averaging area and, by extension, the effect of the ocean surface sampling on the estimated ocean wave spectra might change accordingly.

In this paper, the ocean surface sampling process is addressed and an analytical model is proposed to describe its effect on the estimates of ocean wave spectra. Furthermore, a modulation transfer function, referred to as the Inverse Sampling Averaging Filter (ISAF), is proposed to mitigate the effect of the radar sampling process on the CFT method estimates of ocean wave spectra.

The remainder of this paper is organized as follows. Section II addresses the radar sampling process of the ocean surface, presents an analytical model to describe its effect on the estimates of ocean wave spectra, and proposes the ISAF to mitigate that effect. Section III presents an overview of the field data that are used to validate the performance of the ISAF method. It also presents a performance comparison between the CFT-without-ISAF and the CFT-with-ISAF methods. Conclusions and a brief consideration of continuing directions for this work are presented in Section IV.

II. THE RADAR SAMPLING PROCESS AND THE INVERSE SAMPLING AVERAGING FILTER (ISAF)

A. RADAR SAMPLING PROCESS

To sample the ocean surface over the range dimension in a certain direction using an X-band marine radar, the radar sends out electromagnetic pulses with the main beam pointed in that direction, as shown in Figure 2. Subsequently, the radar starts to repeatedly receive the returned scatter for short periods of time $\tau = 1/f_s$, where f_s is the radar sampling frequency. The radar range resolution Δ_r is determined by τ via [10], [11]

$$\Delta_r = c\tau/2, \tag{1}$$

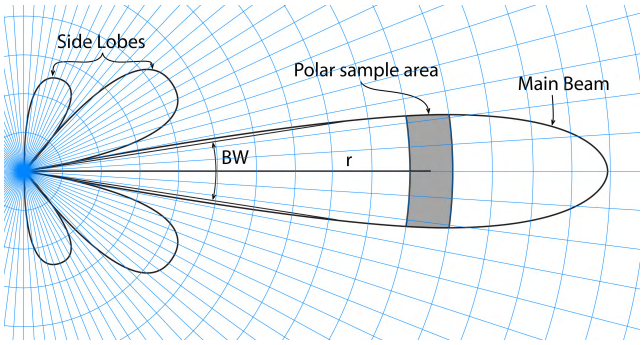

FIGURE 2. An illustration of radar radiation.

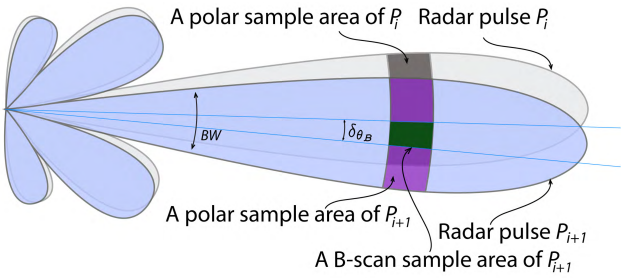

FIGURE 3. An illustration of the polar sample area overlap between consecutive radar pulses.

where c is the speed of light. The azimuth radar resolution is given by

$$\Delta_\theta = BWr,$$

where BW is the beam width and r is the distance of the sample from the radar. The returned scatter from the sample is collected from the entire area of the sample. This implies that an averaging filter is involved in the sampling process. The manner in which different locations in the sample area contribute to the radar output is difficult to estimate since it depends on the ocean state at that moment. However, to simplify the problem we assume that different parts in the sample area contribute equally to the returned scatter.

At an arbitrary range r, a clear distinction should be made between the azimuth radar resolution, which is defined by BW, and the azimuth B-scan resolution, which is defined by the azimuthal shift between two consecutive pulses δ_{θ_B}. Typically, the azimuth B-scan resolution is higher than the azimuth radar resolution, (i.e. $BW > \delta_{\theta_B}$). This results in an overlap between the radar return collecting area of adjacent azimuthal B-scan samples. Figure 3 is an illustration of the overlap between two consecutive radar pulses P_i and P_{i+1}. The higher the azimuth B-scan resolution (i.e smaller δ_{θ_B}) in comparison with the azimuth radar resolution, the more overlap there is between the polar sample areas of adjacent B-scan samples. However, the effect of the averaging filter proposed in this paper on the estimated wave spectra is not expected to vary with the azimuth B-scan resolution since it depends on the radar polar sample area and not the B-scan sample area.

Our preliminary approach to investigating the effect of the ocean surface sampling process on the estimates of the ocean wave spectra is as follows. First, ocean surface elevation Cartesian images are simulated on a fine grid using a Cartesian spatial resolution of 1×1 m^2. Next, B-scan images are generated from the simulated ocean surface elevation Cartesian images using values of Δ_r and BW that are used in an actual X-band marine radar as listed in Table 1. A B-scan sample is calculated by averaging those high-resolution Cartesian samples which fall within the area of the B-scan sample. Finally, the CFT method is used to estimate the ocean wave spectra from the B-scan images.

TABLE 1. Experiment setup: Simulation parameters.

Antenna rotational period	1.44 s
Ocean surface grid resolution	1×1 m^2
Wind wave direction	90° from the true north
The mean period T_{01}	10 s
The significant wave height	3.5 m
The Antenna beam width BW	1°
Pluses per 360°	1000
Radar sampling frequency f_s	20 MHz
Radar range resolution Δ_r	7.5 m

In order to understand the behavior of the ocean surface sampling process, the CFT-estimates are compared to the input spectrum. It must be noted here that neither shadowing nor tilt modulation were implemented in our simulation in order to examine the effect of the ocean surface sampling alone. A modified Pierson-Moskowitz-based power distribution model presented in [12] was adopted to generate the input non-directional wave spectrum of the simulation. A squared cosine distribution [2] was used to add the directional component of the input directional wave spectrum of the simulated images. Furthermore, for more realistic simulation output, wave number phases were drawn from a uniform distribution.

Figure 4a shows an example of the generated simulation input directional wave spectrum based on the parameters listed in Table 1. Figure 4b depicts a sample of the simulated high resolution ocean surface elevation images. Figure 4c shows the B-scan image generated from the high resolution ocean surface image displayed in Figure 4b. A B-scan sample was generated by averaging the high resolution Cartesian image samples located within its corresponding polar sample area. For example, the B-scan sample of P_{i+1} shown in Figure 3 is calculated by averaging the high resolution image samples located in the polar sample area of P_{i+1} shown in the same figure. Figure 4d shows an analysis window of size 1600×800 m generated from the B-scan image displayed in Figure 4c using the scan conversion process outlined in [13]. The analysis window location was arbitrarily chosen at the range and direction of 1000 m and 0°, respectively. It should be noted that the analysis window location should not affect the estimated ocean wave spectra

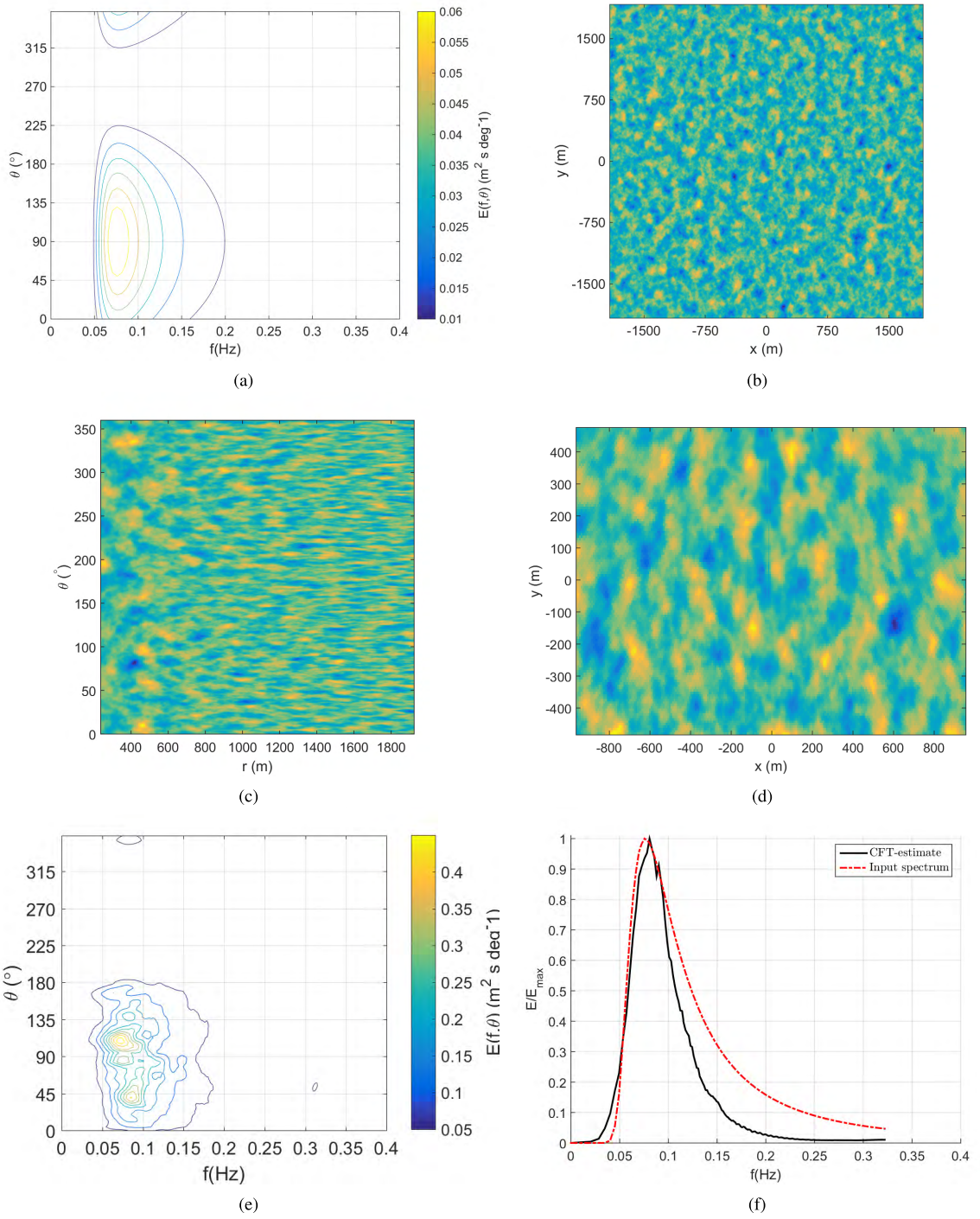

FIGURE 4. A synthetic data example that illustrates the effect of the radar sampling process of the ocean surface on the estimates of ocean wave spectra (a) Simulated input directional wave spectrum. (b) A sample high resolution simulated ocean surface elevation. (c) A sample B-scan image produced from the simulated high resolution image. (d) A selected rectangular analysis window from the scan converted B-scan image. (e) The normalized estimated directional wave spectrum using the CFT method. (f) The normalized input and CFT-estimate of the non-directional wave spectra.

since none of the radar imagining mechanism, including shadowing and tilt modulation, were implemented in the simulation. This conclusion has been reached by using multiple analysis windows, which are located at different ranges and directions, in estimating ocean wave spectra. Similar results were acquired for the tested analysis windows. Figure 4e contains the CFT-estimate of the directional wave spectrum from the analysis window with a sample shown in Figure 4d.

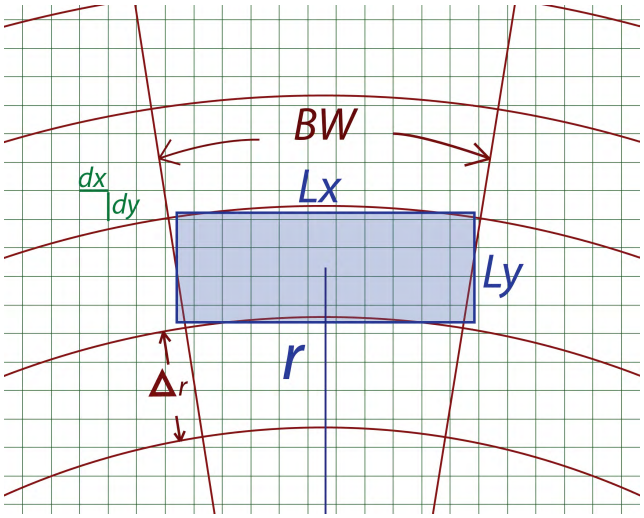

FIGURE 5. An illustration of the the polar sample area, overlaid on the fine grid of resolution *dx* by *dy*.

Also, Figure 4f displays the normalized CFT-estimate of the non-directional wave spectrum compared to the simulated normalized input non-directional wave spectrum. Clearly, the normalized CFT-estimate of the non-directional wave spectrum decays faster than the normalized input spectrum. This supports our assumption that the sampling process may be presented by an averaging (low pass) filter that attenuates high frequencies relative to low frequencies. It should be noted that the plotted estimated wave spectra in Figures 4e and 4f, as well as the rest of figures in this paper, were smoothed using a Gaussian filter to allow better visual comparison. However, no smoothing filters were applied on the estimated ocean wave spectra used in calculating ocean state parameters.

To provide better insight into the effect of the ocean surface sampling on the estimated ocean wave spectra from the simulated data, Figure 5 shows the area of a B-scan sample as a function of the range resolution Δ_r, the beam width BW and the range r. The figure also shows the high-resolution grid for the simulated ocean surface elevation with a spatial resolution of $dx \times dy = 1 \times 1\ \mathrm{m}^2$. Clearly, the number of high-resolution samples that are averaged to form the B-scan sample is not fixed, but is increasing with range r and, by extension, with the area of the B-scan sample. To simplify the problem, the B-scan area can be considered to be rectangular with the dimensions of $L_x \times L_y$, where $L_x = r\ BW$ and $L_y = \Delta_r$ instead of being a ring sector, as shown in Figure 5. Then, the number of high-resolution samples that are averaged to produce the B-scan sample is given by N_x and N_y, where

$$N_x = \left\lceil \frac{L_x}{dx} \right\rceil \text{ and } N_y = \left\lceil \frac{L_y}{dy} \right\rceil, \tag{2}$$

respectively, where $\lceil \cdot \rceil$ is the ceiling function. For example, using the radar configuration given in Table 1 and Equations 1 and 2 and considering $r = 1000$ m, N_x and N_y are found to be 18 and 8, respectively. The frequency response of this

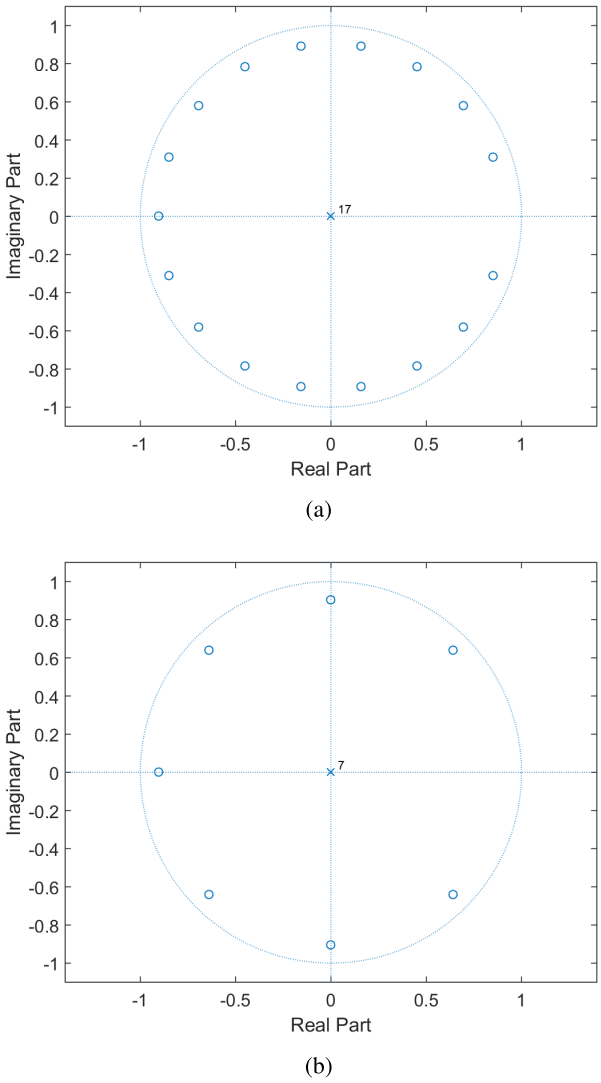

FIGURE 6. Zero-pole plot of the directional filters (a) $H_{\tilde{k}_x}$ and (b) $H_{\tilde{k}_y}$.

averaging process can be given by the low pass filter $H_{\tilde{k}} = H_{\tilde{k}_x} H_{\tilde{k}_y}$ where the directional filters are

$$H_{\tilde{k}_x}(\tilde{k}_x) = \frac{1}{N_x} \sum_{n_x=0}^{N_x-1} (r_z e^{j\tilde{k}_x})^{-n_x} \tag{3}$$

$$H_{\tilde{k}_y}(\tilde{k}_y) = \frac{1}{N_y} \sum_{n_y=0}^{N_y-1} (r_z e^{j\tilde{k}_y})^{-n_y} \tag{4}$$

where $\tilde{k}_x = k_x dx$ and $\tilde{k}_y = k_y dy$ are the normalized wave number vector components in the x and y direction, respectively, and r_z is the magnitude of the filter zeros in the z-plane. In order to achieve an invertible filter, r_z was chosen to be 0.9 (see Section II-C). For $N_x = 18$ and $N_y = 8$, Figures 6a and 6b show the zero-pole diagram of $H_{\tilde{k}_x}$ and $H_{\tilde{k}_y}$, respectively, while Figure 7b shows the normalized

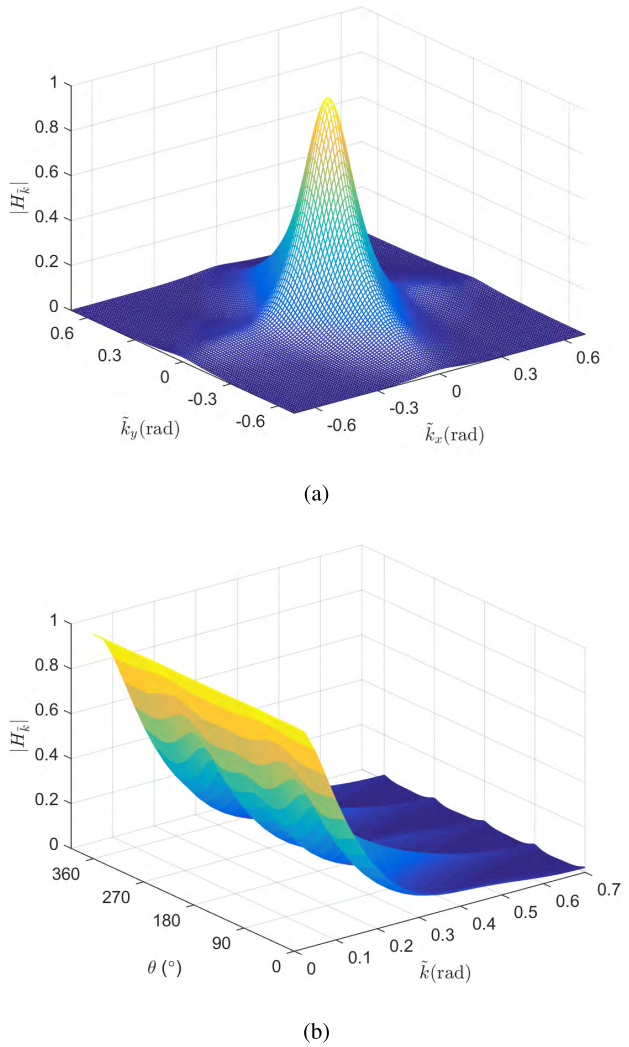

FIGURE 7. The directional frequency response of $H_{\tilde{k}}$ in (a) $\tilde{k}_x, \tilde{k}_y$ and (b) $\tilde{k}, \theta$ domains.

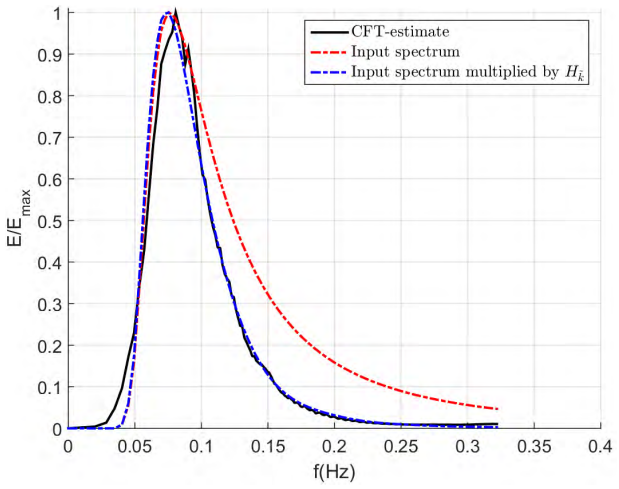

FIGURE 8. The modified (multiplied by $H_{\tilde{k}}$) input non-directional wave spectrum overlaid by the CFT-estimate of the non-directional wave spectrum.

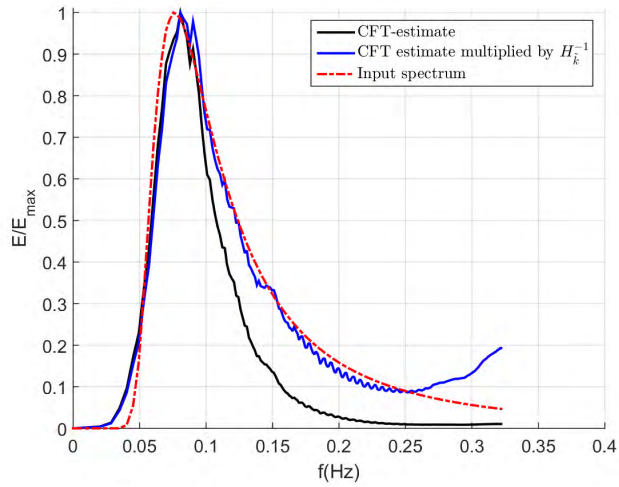

FIGURE 9. Improvement in CFT-estimate using simulated data by multiplying the non-directional ocean wave spectrum by $H_{\tilde{k}}^{-1}$.

directional frequency response of $H_{\tilde{k}}$ in the (k, θ) domain. It can be seen in Figures 6a and 6b that the zeros located at $r = 0.9$ are arranged within the unit circle, thus allows stable filter inverses. It can be also noted from Figures 6a and 6b that the number of zeros in $H_{\tilde{k}_x}$ is higher than in $H_{\tilde{k}_y}$. This is due to the fact that the number of samples, N_x, that are averaged in the x-direction is higher than the number, N_y, in the y-direction. To verify our rectangular area assumption, $H_{\tilde{k}}(\tilde{k}_x, \tilde{k}_y)$ is multiplied by the input directional wave spectrum to produce a modified input non-directional wave spectrum which is compared to the CFT-estimate of the non-directional wave wave spectrum as shown in Figure 8. Clearly, introducing $H_{\tilde{k}}$ improves the agreement between the two non-directional wave spectra. Since $H_{\tilde{k}}$ is invertible, the effect of the radar sampling process may be mitigated by multiplying the CFT-estimate of the directional wave spectrum by $H_{\tilde{k}}^{-1}$. Figure 9 shows the improvement that $H_{\tilde{k}}^{-1}$ brings to the CFT-estimate of the non-directional wave spectrum.

The previous example and the design of $H_{\tilde{k}}$ have been presented with the intention of helping to understand the effect of the ocean surface sampling process on the estimated ocean wave spectra. $H_{\tilde{k}}^{-1}$ was designed to mitigate the effect of the averaging process of the simulated ocean surface elevation with $dx \times dy = 1$ m^2. Considering a higher resolution of the simulated ocean surface elevation leads to higher values of N_x and N_y given in Equation 2 and, hence, to a more accurate design of $H_{\tilde{k}}$ in modeling the effect of the ocean surface sampling process. Ultimately, most accurate design of $H_{\tilde{k}}$ is achieved when $dx \times dy \to 0$, which requires to consider the filter design in the analog domain.

B. THE AVERAGING PROCESS IN THE ANALOG DOMAIN

In order to extend $H_{\tilde{k}}$ to be applicable to radar field data, the filter design has to be considered in the analog domain.

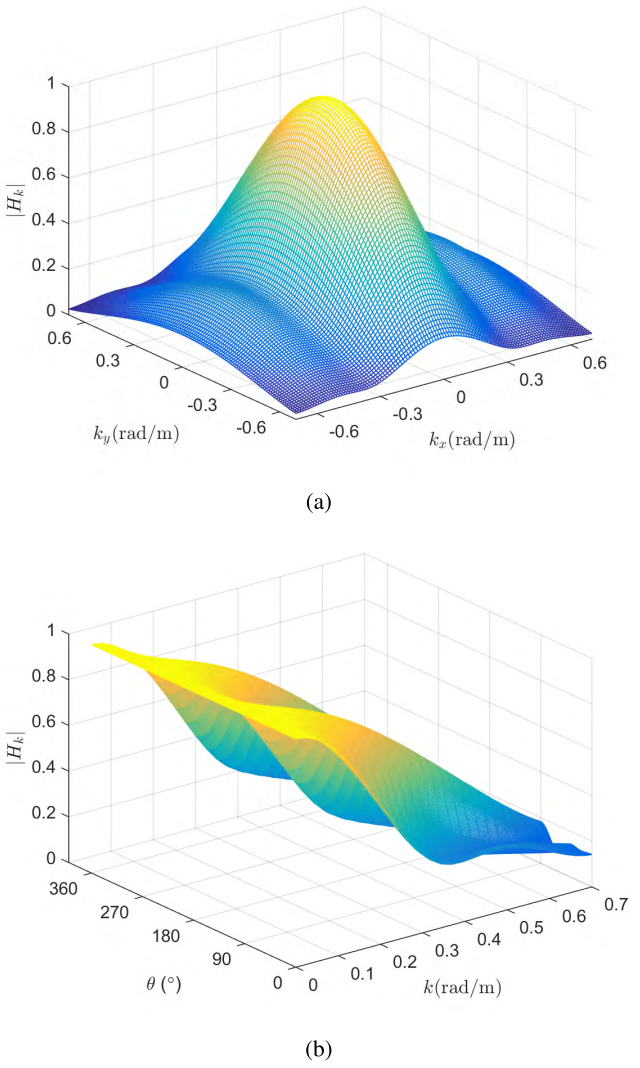

FIGURE 10. The analog directional frequency response of H_k in (a) k_x, k_y and (b) k, θ domains.

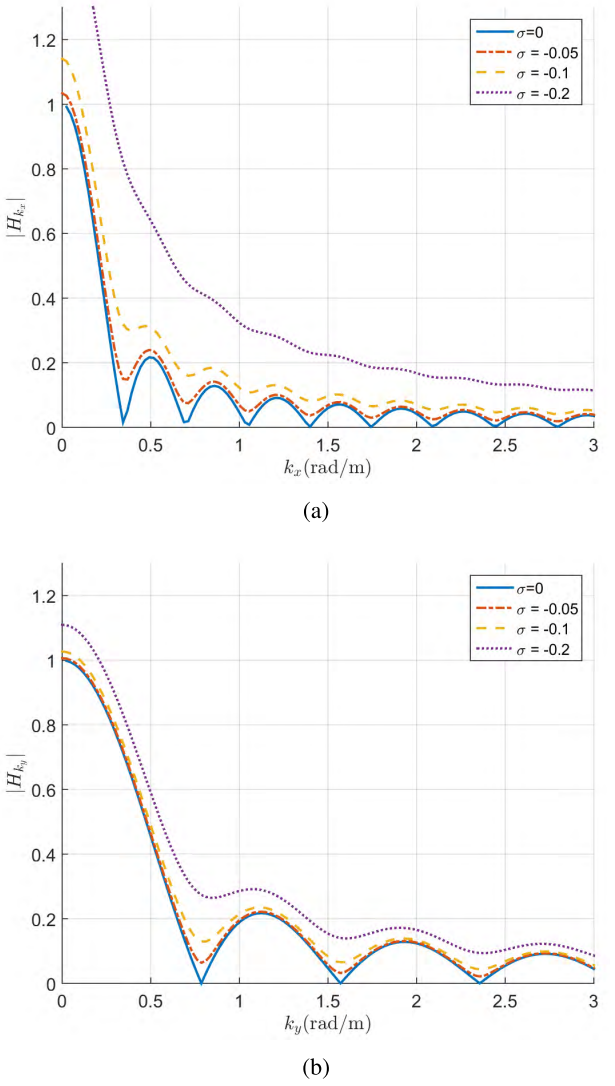

FIGURE 11. The magnitude response of the analog filter (a) H_{k_x}, (b) H_{k_x}, for $\sigma = 0, -0.05, -0.1$ and -0.2.

The radar actually collects the returned scatter from the continuous rectangular area $L_x \times L_y$ shown in Figure 5. Therefore the analog average filter is given by $H_k = H_{k_x} H_{k_y}$ where H_{k_x} and H_{k_y} are integrating filters in the x and y directions, respectively, that may be modelled in the x-direction by a moving average filter in the spatial domain given by rectangular window impulse response:

$$h_x(x) = \frac{1}{L_x} u(x + L_x/2) u(-x + L_x/2).$$

where $u(\cdot)$ is the unit step function. Using the Laplace transform,

$$H_{k_x}(k_x) = \int_{-\infty}^{\infty} h_x(x) \mathrm{e}^{-sx} dx = \frac{\mathrm{e}^{s_x L_x/2} - \mathrm{e}^{-s_x L_x/2}}{s_x L_x} \quad (5)$$

where $s_x = \sigma + jk_x$, with σ being the attenuation constant. Similarly, in the y-direction,

$$H_{k_y}(k_y) = \frac{\mathrm{e}^{s_y L_y/2} - \mathrm{e}^{-s_y L_y/2}}{s_y L_y} \quad (6)$$

where $s_y = \sigma + jk_y$. Using the parameters given in Table 1 and considering $\sigma = -0.1$ for an invertible analog filter (see Section II-C), Figure 10a and Figure 10b show the directional wave number response of H_k in the (k_x, k_y) and (k, θ) domain, respectively. Since H_k is invertible, $H_k^{-1} = 1/H_k$ can be used to mitigate the effect of the radar sampling process on radar field data. H_k^{-1} is referred to as the Inverse Sampling Averaging Filter (ISAF). For radar field data, the CFT alone (i.e. CFT-without-ISAF) uses the modulation transfer function $MTF = k^{-1.2}$ proposed in [2]. On the other hand, the CFT-with-ISAF method proposed in this paper implements the ISAF with the MTF as follows.

$$E_c(\mathbf{k}) = k^{-1.2} E_k(\mathbf{k}) H_k^{-1}(\mathbf{k}).$$

where E_c is the corrected estimate of the directional wave spectrum and E_k is the estimated directional wave spectrum using the CFT method.

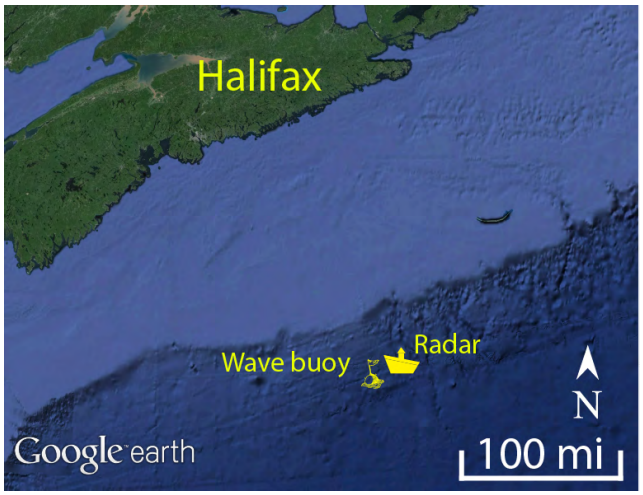

FIGURE 12. Locations of wave buoy and radar during the experiment of data collection near Halifax, Nova Scotia, on the east coast of Canada on Dec. 01, 2008.

C. FILTER INVERSION AND THE ATTENUATION CONSTANT σ

Using the attenuation constant $\sigma = 0$ in Equations 5 and 6 produces a non-invertible wave number response due to the zeros shown in the $\sigma = 0$ magnitude response in Figures 11a and 11b, respectively. The zero locations determine the shape of the filter. Since the averaging process covers a longer range in the x-direction compared to the y-direction, it can be seen in Figures 11a and 11b that $|H_{k_x}|$ has more zeros and a smaller pass-band width than $|H_{k_y}|$. If $\sigma = 0$, H_k is non-invertible because once the radar averages the returned scatter from all positions in the sample area, information about individual positions cannot be retrieved from the radar output. Still, we can use an approximation of the filter by setting $\sigma = -0.1$ in Equations 5 and 6. This value was chosen so that the approximation follows the envelope of the original filter with $\sigma = 0$ as shown in Figures 11a and 11b. Choosing a smaller value of σ, such as -0.2, might lead to an underestimation of wave spectra components at low wave numbers due to the high amplitude response of $|H_{k_x}|$ at those wave numbers as depicted in Figure 11a. On the other hand, using a higher value of σ such as -0.05 might lead to an unstable behavior of the inverse filters due to small values of $|H_{k_x}|$ and $|H_{k_y}|$ at their zeros. For the same reason, $r = 0.9$ was used in Equations 3 and 4. This value was found using the Z-Laplace transform relationship theory [14], where

$$z = r_z e^{j\tilde{k_x}} = e^{s_x dx} = e^{(\sigma + jk_x)dx} = e^{\sigma dx} e^{jk_x dx}.$$

Therefore, $r_z = e^{\sigma dx}$. Using $\sigma = -0.1$ and $dx = 1$ m as shown in Table 1 leads to $r = 0.9$.

III. RESULTS AND ANALYSIS

A. EXPERIMENT SETUP AND DATA OVERVIEW

In this paper, field data collected over a 10-day period were used to validate the performance of the ISAF method. The data were acquired using two shipborne X-band marine radars that operated at 9.4 GHz and HH polarization. Figure 12 shows the location where the data were collected near Halifax, Nova Scotia, off the east coast of Canada. Estimates of ocean wave spectra and sea state parameters were generated using the CFT-with-ISAF method and compared to the estimates generated using CFT-without-ISAF method. Furthermore, the results from both methods are compared to ground truth estimates that were generated by a TRIAXYS Wave Rider buoy. It must be noted that the buoy drifted from its original location for about 41 km during the 10-day period of the experiment. However, the drift in the buoy's location has no apparent effect on the analysis presented in this paper since the radars were well offshore and always within a 10 km distance of the buoy. The buoy generated a directional wave spectrum estimate every 30 minutes with a resolution of 0.005 Hz in the frequency dimension and 3° in the azimuth dimension. Since the radar antenna rotation period was 1.44 s, the non-directional ocean wave spectrum estimates generated using the CFT-with-ISAF method and CFT-without-ISAF method were limited to the range of 0.05 to 0.35 Hz. Further radar and experimental setup details are listed in Table 2.

TABLE 2. Experiment setup: Radar and buoy parameters.

Experiment location	42°22.4391N 61°55.5654W
Antenna rotational time	1.44 s
Antenna height	10 m
Sampling frequency	20 MHz
Water depth	200 m
Polarization	Horizontal
TRIAXYS wave period accuracy	better than 1%
TRIAXYS wave direction accuracy	1°

In our analysis, a single CFT-estimate of the directional wave spectrum required 32 B-scan images. First, the 'scan conversion' process is used to convert the B-scan images to Cartesian images [15]. Next, three rectangular analysis windows are selected. Each analysis window, $I(\xi)$, where $\xi = (x, y, t)$ is the space-time vector, had a size of 256×128×32 samples with a spatial resolution of 7.5 m/sample in the x and y dimensions and a time resolution of 1.44 s. This size of analysis window was chosen over other popular sizes, e.g. 128×128×32, to cover a larger azimuth range in order to mitigate the dependency of wave spectral estimation on the azimuthal dimension. The convention of uniformly distributing the analysis windows over the field of view, which is 360° for our data, is adopted [16]. The analysis windows are placed at 0°, 120° and 240°. However, it should be noted that a previous study by Lund *et al.* [6] suggested to place the analysis windows in the up-wave direction which allows for higher *SNR*. Also, the authors of this paper suggested in a previous study [7] to place the analysis windows in the up-wave directions of the ocean wave system using a method referred to as the Adaptive Recursive Positioning Method (ARPM) in order to allow for better ocean wave spectral estimation.

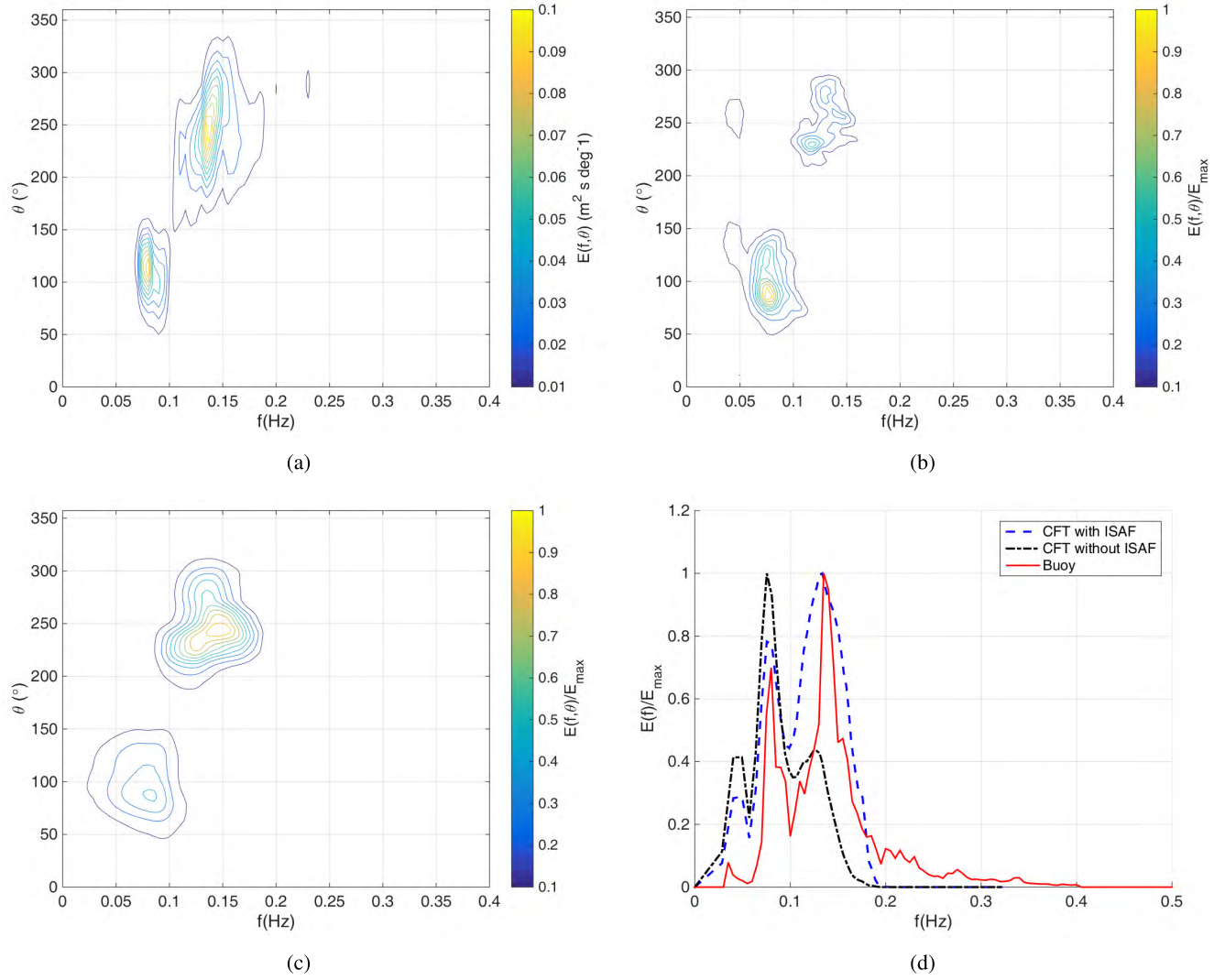

FIGURE 13. A field data example demonstrating the improvement introduced by the ISAF to the CFT-method in ocean wave spectral estimation. Data were recorded on Nov 29, 2008 at 1:10 PM. The recorded significant wave height and wind speed were 2.56 m and 25.5 kts, respectively: (a) The ground truth directional wave spectrum estimated using the TRIAXYS Wave Rider buoy data. (b and c) The directional wave spectrum estimated using the CFT-without-ISAF and the CFT-with-ISAF method, respectively. (d) The non-directional wave spectra estimated using the CFT-without-ISAF, the CFT-with-ISAF method, and the TRIAXYS Wave Rider buoy data.

The analysis windows were all centred at a range of 1000 m, which is around the nearest range available in our data. Even though the ISAF may have more effect in the far range due to the larger values of Lx, our analysis was limited to near range since the performance of the CFT method is better at near ranges compared to far ranges due to the smaller shadowing effect and stronger radar return power. In [6], it was found that the *SNR* was higher at near range compared to mid and far ranges. Also, the radar imaging effect proposed in this paper suggests that the near range parts of the radar image should less suffer from the radar averaging sampling process. Furthermore, the effect of radar sampling process acts upon the radar image in addition to shadowing and tilt modulation. Since the effect of shadowing and tilt modulation on the estimated wave spectra using X-band radar images is not fully understood, it makes sense to perform the ISAF validation comparisons using the near range where shadowing is minimum.

The 3D Cartesian Fourier Transform (CFT) was performed on each analysis window $I(\xi)$ to produce the 3D image spectrum $F(\Omega)$, where Ω is the three-dimensional wave number-frequency vector (k_x, k_y, ω) with k_x and k_y being the spatial wave vector components and $\omega = 2\pi f$ the wave angular frequency. The directional wave spectrum $E(\omega, \theta)$, where θ is the azimuth angle, and the non-directional $E(\omega)$ wave spectrum were computed from $F(\Omega)$ and averaged from the three analysis windows [2], [7]. Subsequently, sea state parameters, including the peak wave period T_p, the mean period T_{01}, the zero-crossing wave period T_z, the peak wave direction θ_p, and the significant wave height H_s were estimated using

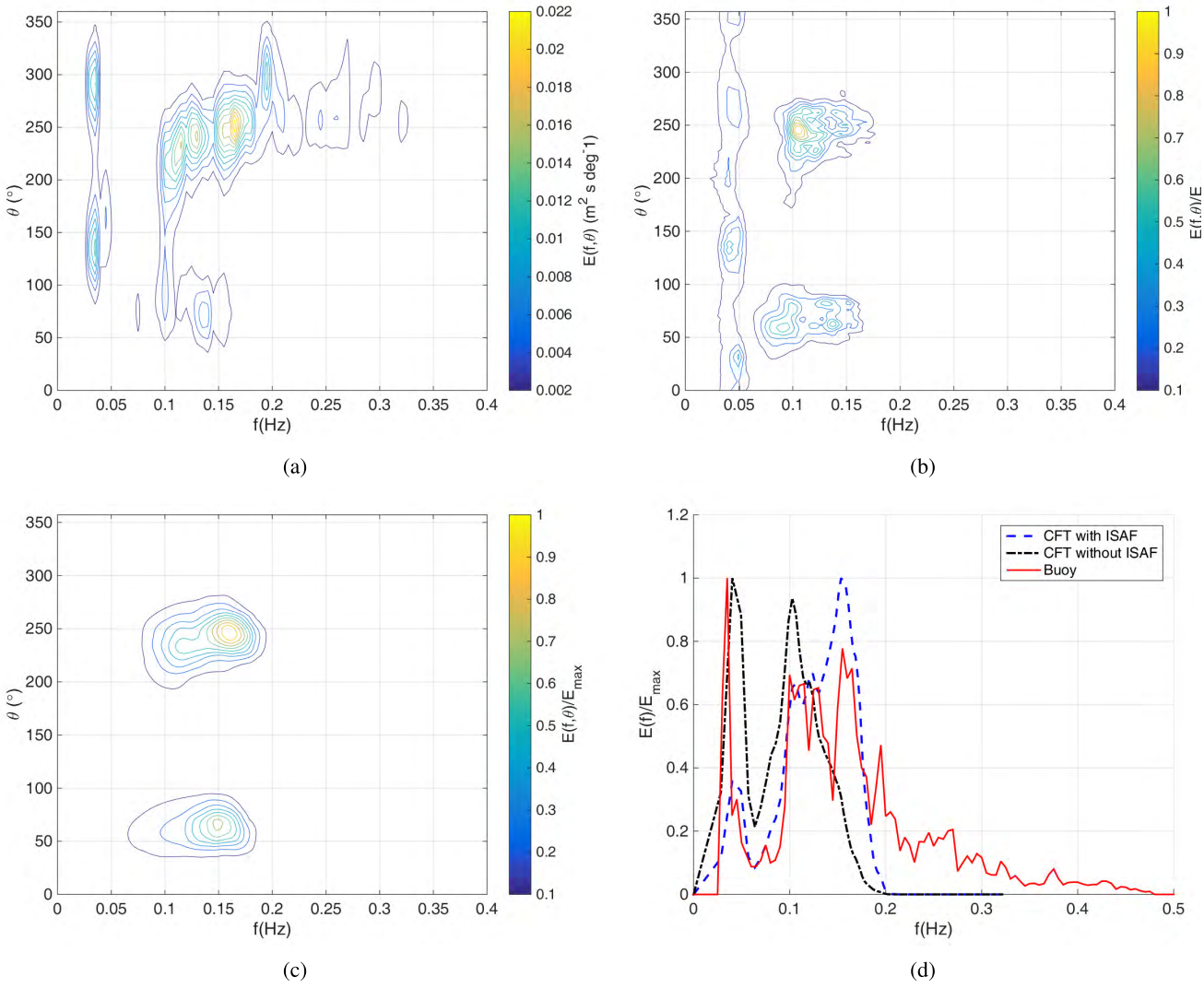

FIGURE 14. A field data example demonstrating the improvement introduced by the ISAF to the CFT-method in ocean wave spectral estimation. Data were recorded on Dec 4, 2008 at 12:00 PM. The recorded significant wave height and wind speed were 1.53 m and 10.8 kts, respectively: (a) The ground truth directional wave spectrum estimated using the TRIAXYS Wave Rider buoy data. (b and c) The directional wave spectrum estimated using the CFT-without-ISAF and the CFT-with-ISAF method, respectively. (d) The non-directional wave spectra estimated using the CFT-without-ISAF, the CFT-with-ISAF method, and the TRIAXYS Wave Rider buoy data.

$E(\omega, \theta)$ and $E(\omega)$ [17]. Finally, for a proper comparison with the wave buoy output, a buoy wave spectrum estimate was compared to the average of all CFT wave spectral estimates that were produced within that 30-minute interval.

B. FIELD DATA EXAMPLES

In this section, in order to demonstrate the performance of the ISAF, three field data examples of ocean wave spectral estimation using the CFT-with-ISAF method and the CFT-without-ISAF method are presented. Figure 13 shows (a) a ground-truth directional wave spectrum estimated from TRIAXYS Wave Rider buoy data, (b) the estimated directional wave spectrum using the CFT-without-ISAF, (c) the estimated directional wave spectrum using the CFT-with-ISAF method, and (d) the non-directional wave spectra deduced from the three directional wave spectra. In the case of a directional wave spectrum with multiple peaks, the terminology being used here is that the peak with the highest peak energy is referred to as the main peak, while the other peaks are referred to as the secondary peaks. Also, since we are dealing with normalized wave spectra, the energy level of the secondary peaks is measured with respect to the energy level of the main peak of the same spectrum. Figures 13a and 13d show that the ground truth wave spectra have a main peak at 0.135 Hz and 243° and a secondary peak at 0.08 Hz and 114° with relative energy level of 70%. Looking at the estimates of the directional and non-directional wave spectrum that are generated using the CFT-without-ISAF method shown in Figures 13b and 13d, respectively, both peaks were detected. However, the main

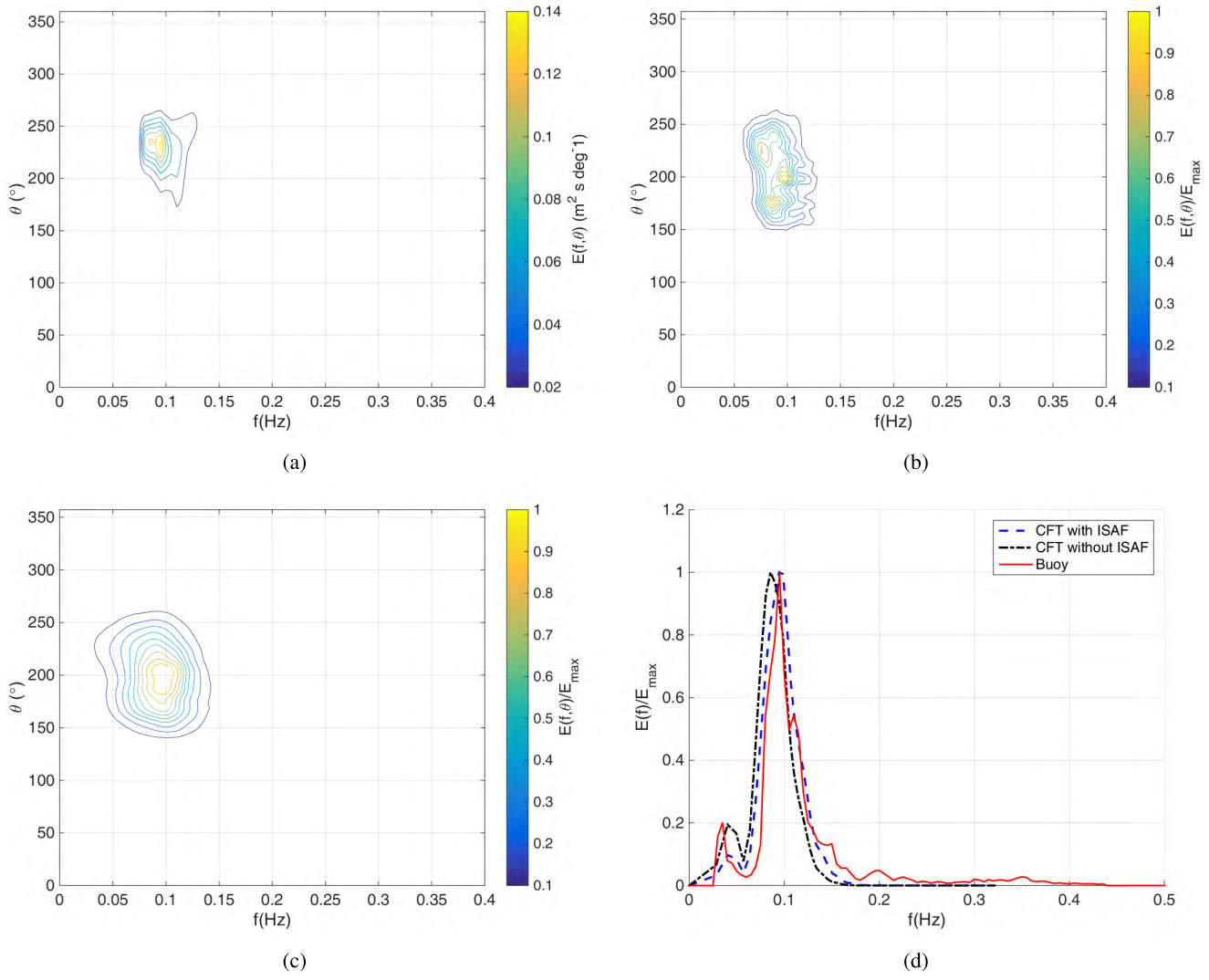

FIGURE 15. A field data example demonstrating the improvement introduced by the ISAF to the CFT-method in ocean wave spectral estimation. Data were recorded on Dec 01, 2008 at 12:30 PM. The recorded significant wave height and wind speed were 2.47 m and 24.8 kts, respectively: (a) The ground truth directional wave spectrum estimated using the TRIAXYS Wave Rider buoy data. (b and c) The directional wave spectrum estimated using the CFT-without-ISAF and the CFT-with-ISAF method, respectively. (d) The non-directional wave spectra estimated using the CFT-without-ISAF, the CFT-with-ISAF method, and the TRIAXYS Wave Rider buoy data.

peak was barely detected and was detected as the secondary peak at 0.128 Hz and 245° with a relative energy level of 43%, while the secondary peak was detected as the main peak at 0.075 Hz and 100°. On the other hand, when the ISAF was implemented in the CFT method, both peaks were properly detected as shown in Figures 13c and 13d. The main peak was detected as the main peak at 0.134 Hz and 245° and the secondary peak was detected as a secondary peak at 0.075 Hz and 100° with a relative energy level of 78%. Clearly, the ISAF has significantly improved the wave spectrum estimation in this example. Figure 13d also shows better agreement between the ground truth non-directional spectrum and the spectrum obtained by the CFT-with-ISAF method compared to the CFT-without-ISAF.

The same conclusion may be drawn from the example given in Figure 14. The ground truth directional wave spectrum shown in Figure 14a contains four peaks located at 0.03 Hz and 140°, 0.03 Hz and 290°, 0.14 Hz and 75°, and 0.16 Hz and 250°. For discussion convenience, these peaks are referred to as P1, P2, P3, and P4. It can be seen from Figures 14b and 14c that P1 and P2 were not detected by CFT-with-ISAF and detected by the CFT-without-ISAF. However, P3 and P4 were detected more accurately in terms of peak location and relative energy as shown in Figure 14d. Since most of the spectrum energy is actually contained in P3 and P4, it can be concluded that the CFT-with-ISAF outperforms the CFT-without ISAF in this example too.

Finally, Figure 15 shows another example for comparison between the CFT-with-ISAF and CFT-without-ISAF. In this example, non-directional wave spectrum estimates generated using both methods show a good agreement with the non-directional ground truth wave spectrum as shown

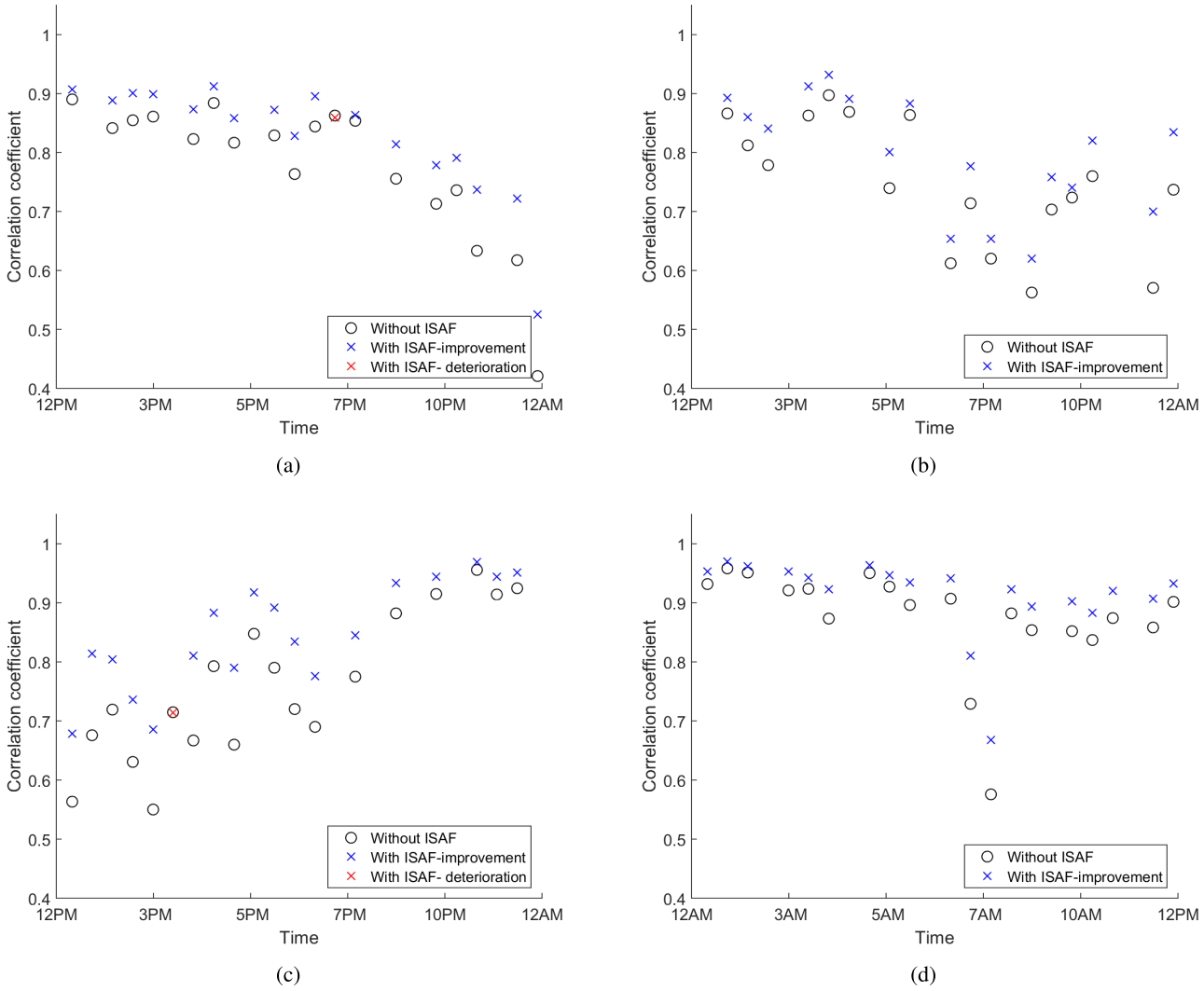

FIGURE 16. A comparison of the CFT with and without the ISAF in terms of the respective wave frequency spectrum similarity with respect to the buoy ground truth spectra. Each point represents the correlation coefficient between ground truth and the radar data 30 minute averaged frequency wave spectra. (a) Dec 1 afternoon and evening, (b) Dec 2 afternoon and evening, (c) Dec 3 afternoon and evening, (d) Dec 4 morning.

in Figure 15d. However, the CFT-with-ISAF estimate shows a slight advantage for the CFT-with-ISAF estimate in terms of agreement with the ground truth non-directional wave spectrum.

C. PERFORMANCE VALIDATION

The performance validation methodology used in this paper is based on the accuracy of the non-directional wave spectrum estimates $E(\omega)$, the peak wave period T_p, the mean wave period T_{01}, the zero-crossing wave period T_z, the peak wave direction θ_p, and the significant wave height H_s. The accuracy of the non-directional wave spectrum estimate E_R with respect to a ground truth non-directional wave spectrum E_B is measured by the correlation coefficient value ρ between the two spectra. The correlation coefficient value ρ is defined by

$$\rho = \frac{N_f \sum E_R E_B - (\sum E_R)(\sum E_B)}{\sqrt{[N_f \sum E_R^2 - (\sum E_f)^2][N_f \sum E_B^2 - (\sum E)^2]}}, \quad (7)$$

where N_f is the number of frequency points in E_R and E_B. The correlation coefficient value ρ increases with the agreement between the two spectra and approaches 1 when the two spectra are identical, which occurs rarely in practice. On the other hand, ρ takes a minimum value of 0 when there is no similarity between the two spectra. The estimation accuracy of the sea state parameters T_p, T_{01}, T_z, θ_p, and H_s, which are estimated from the directional and non-directional wave spectra as outlined in [3] and [17], is measured by the mean absolute error of their estimates. The estimation mean absolute error $\overline{|\varepsilon_\chi|}$ (where here χ represents, variably, T_p, T_{01}, T_z, θ_p or H_s) is given by

$$\overline{|\varepsilon_\chi|} = \frac{1}{N} \sum_{n=1}^{N} |\chi_n - \chi_{B_n}|, \quad (8)$$

where N is the total number of radar estimates and χ_B is the ground truth of χ as collected by the ground truth.

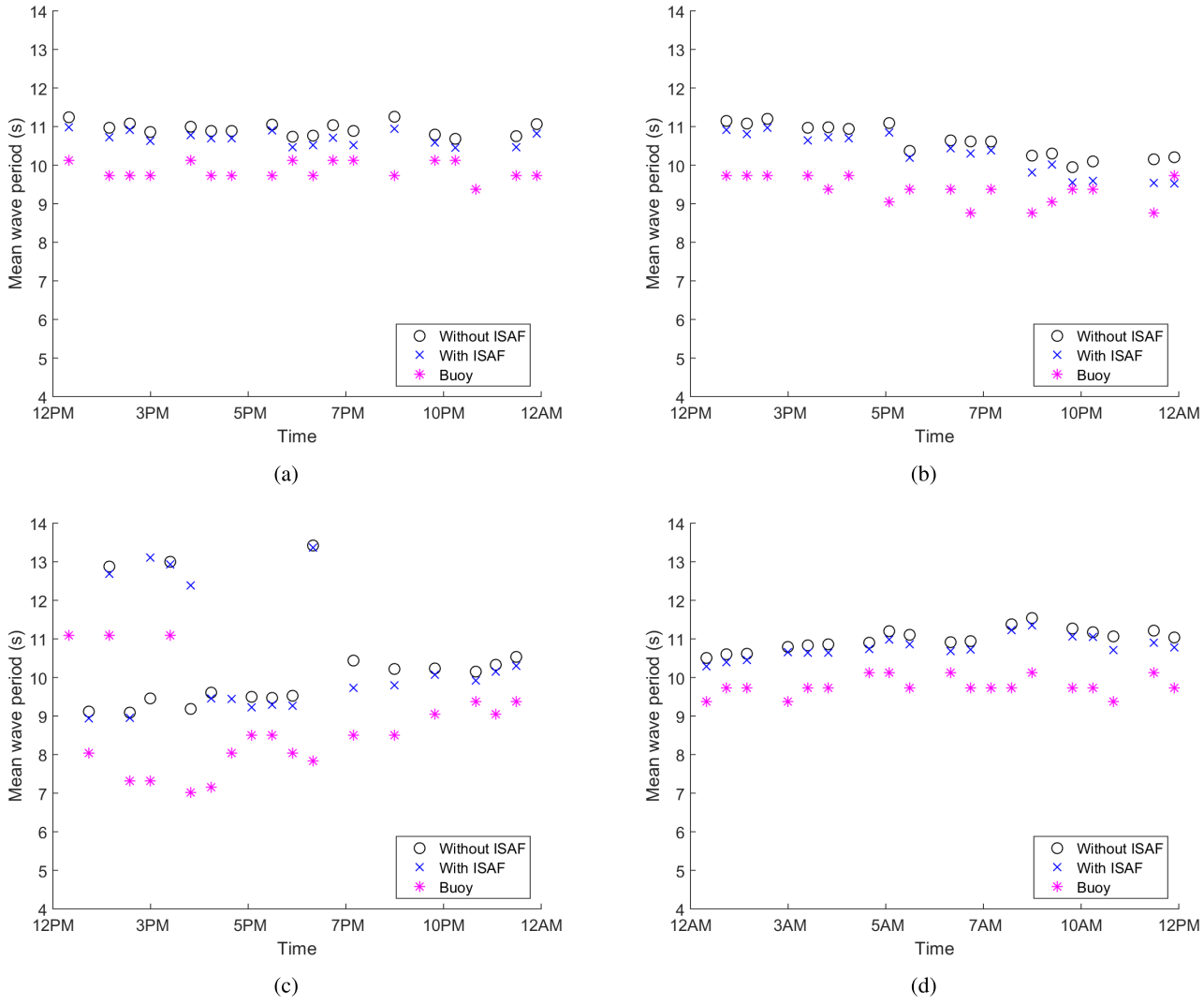

FIGURE 17. A comparison of the CFT with and without the ISAF in terms of the mean wave period. (a) Dec 1 afternoon and evening, (b) Dec 2 afternoon and evening, (c) Dec 3 afternoon and evening, (d) Dec 4 morning.

Also, the error standard deviation σ_ε of estimates of each of T_p, T_{01}, T_z, θ_p and H_s is calculated to demonstrate how the estimates are distributed around the ground truth estimate value. The estimation error standard deviation $\sigma_{\varepsilon_\chi}$ is given by

$$\sigma_{\varepsilon_\chi} = \sqrt{\frac{1}{N}\sum_{n=1}^{N}\left(\chi_n - \frac{1}{N}\sum_{m=1}^{N}\chi_m\right)^2}. \tag{9}$$

In order to examine the performance improvement introduced to the CFT method by the ISAF, ocean wave spectra were estimated from the 10-day collected field data described in Section III-A using the two methods: CFT-without-ISAF and CFT-with-ISAF. Subsequently, the sea state parameters T_p, T_{01}, T_z, θ_p, and H_s were calculated for those estimates. The correlation coefficient ρ is calculated for the non-directional wave spectra that are generated using the CFT-without-ISAF and CFT-with-ISAF methods. Figure 16 shows results of ρ in pairs for four 12-hour periods from the 10-day data collected. These are denoted as the CFT-without-ISAF coefficient ρ, which is marked using a 'o ', and the CFT-with-ISAF coefficient ρ, which is marked using a '×'. Also, the results of the CFT-with-ISAF method are plotted in blue or red to indicate improvement or deterioration, respectively, compared to the results from the CFT-without-ISAF method. Clearly, the performance of the CFT is significantly improved with the implementation of the ISAF. This can be seen from Figure 16 with most of the CFT-with-ISAF values of the correlation coefficient being higher than the values obtained using the CFT-without-ISAF method. An average improvement in the correlation coefficient value, hence the accuracy of ocean wave spectra estimation, of 11% has been achieved. It can be expected that this improvement will reflect positively on the estimation accuracy of sea state parameters. Figure 16a shows a descending trend in the performance of the CFT-with-ISAF as well as

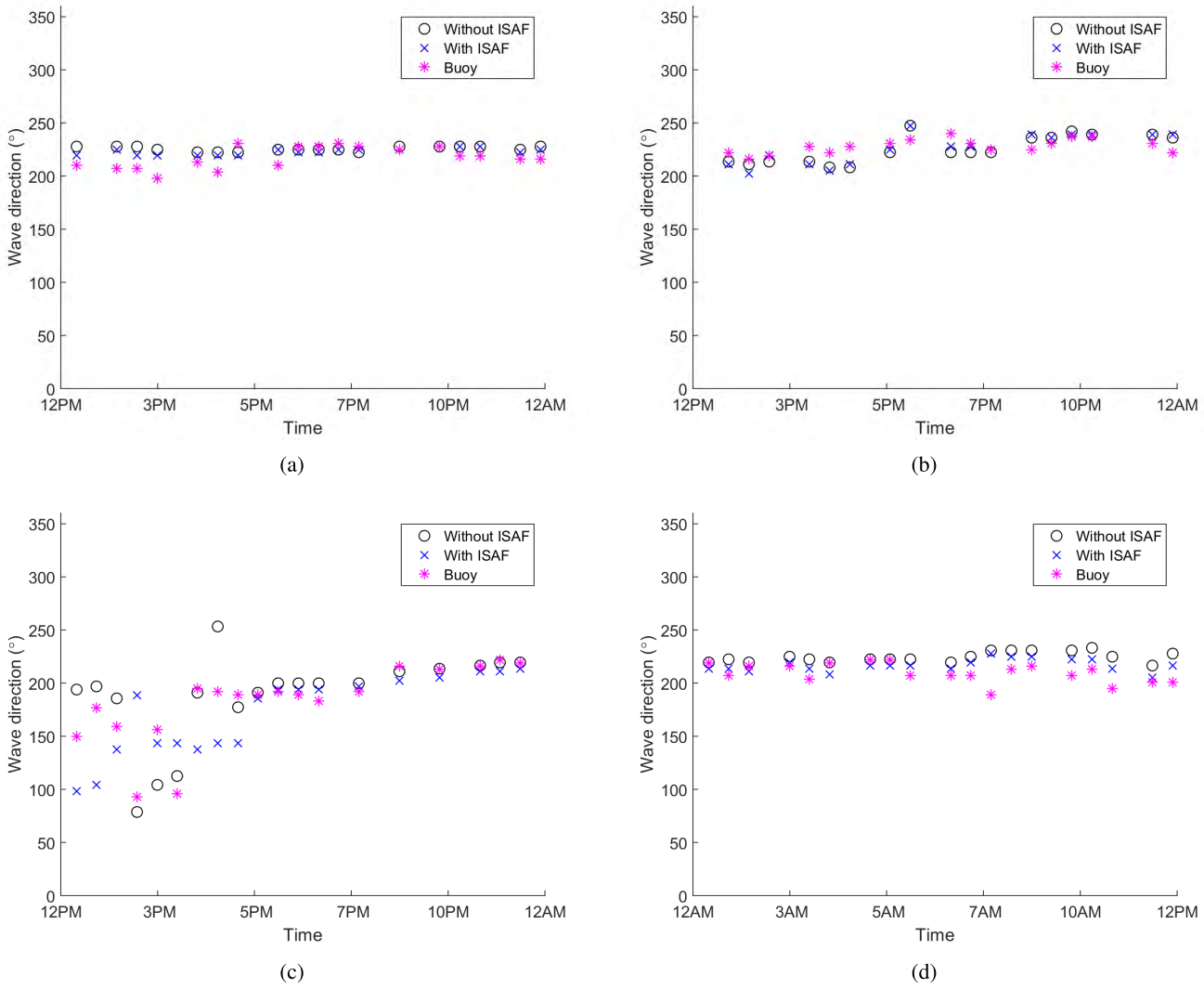

FIGURE 18. A comparison of the CFT with and without the ISAF in terms of the wave peak direction. (a) Dec 1 afternoon and evening, (b) Dec 2 afternoon and evening, (c) Dec 3 afternoon and evening, (d) Dec 4 morning.

the CFT-without-ISAF. This trend indicates a deterioration in the radar recorded images quality for estimating ocean wave spectra. The change in the radar image quality might be contributed to various reasons such as changes in wind speed and direction, precipitation, fog, the sea state, or the ocean wave contributing systems (wind waves, swell or both). However, the effect of the weather condition on the estimation of ocean wave spectral analysis is out of the scope of this paper.

Here, we further validate the performance of the CFT-with-ISAF method against the CFT-without-ISAF method by using both to estimate T_p, T_{01}, T_z, θ_p and H_s. Figures 17 and 18 show four 12-hour periods of results for T_{01} and θ_p, respectively. Furthermore, the mean absolute error $\overline{|\varepsilon_\chi|}$ and the error standard deviation $\sigma_{\varepsilon_\chi}$, where $\chi = T_p, T_{01}, T_z, \theta_p$ and H_s, are calculated for the CFT-without-ISAF and CFT-with-ISAF method using the 10-day field dataset described in Section III-A. Results are listed in Table 3. Once again, the improvement from using the ISAF is observed in estimating sea state parameters. For $\overline{|\varepsilon_{T_p}|}$, $\overline{|\varepsilon_{T_{01}}|}$, $\overline{|\varepsilon_{T_z}|}$, and $\overline{|\varepsilon_{\theta_p}|}$, improvements of 12%, 21%, 17%, and 34% were achieved. Figure 17 shows a consistent over-estimation in the wave period using both the CFT-with-ISAF and CFT-without-ISAF in comparison to the buoy estimates. This over-estimation is due to the Modulation Transfer Function used in this paper, $MTF = k^{-1.2}$. This MTF is an empirical function that was developed to compensate for the distortion in the estimated wave spectra using X-band radars due to shadowing and tilt modulation [2]. Even though this MTF is widely accepted in the literature, some studies have shown that using the exponent of -1.2 in the MTF may be more accurate for some field data than for others [8]. Therefore, using a different exponent might work better for some data, but could also cause a consistent overestimation

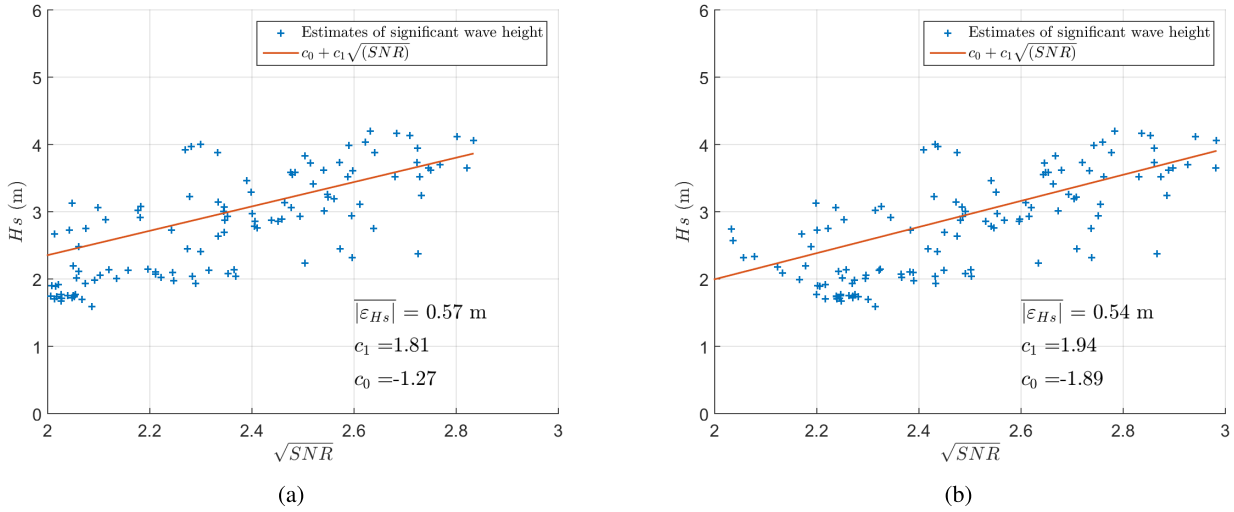

FIGURE 19. The estimates of significant wave height using (a) the CFT-without-ISAF and (b) the CFT-with-ISAF.

TABLE 3. Comparison of the CFT with and without the ISAF in wave period and peak direction estimation.

	$\overline{\lvert\varepsilon_{T_p}\rvert}$(s)	$\sigma_{\varepsilon_{T_p}}$ (s)	$\overline{\lvert\varepsilon_{T_{01}}\rvert}$(s)	$\sigma_{\varepsilon_{T_{01}}}$ (s)	$\overline{\lvert\varepsilon_{T_z}\rvert}$(s)	$\sigma_{\varepsilon_{T_z}}$(s)	$\overline{\lvert\varepsilon_{\theta_p}\rvert}$(°)	$\sigma_{\varepsilon_{\theta_p}}$(°)	$\overline{\lvert\varepsilon_{H_s}\rvert}$(m)	$\sigma_{\varepsilon_{H_s}}$(m)
CFT-without-ISAF	2.5	0.9	2.4	0.8	2.3	0.8	15.1	16.1	0.57	0.73
CFT-with-ISAF	2.2	0.5	1.9	0.5	1.9	0.5	9.9	6	0.54	0.69

or underestimation in the wave period on other data depending on how far the exponent used in the *MTF* is from an optimal value. However, the effect of shadowing, tilt modulation and the *MTF* are out the scope of this paper.

It should be noted in Figure 17c that unlike the rest of the buoy readings in the figure, the readings during the period of 12:00 PM - 3:30 PM fluctuate inconsistently. The reason for these fluctuations is unlikely to be due to an error in the buoy itself since a corresponding fluctuation is also found in the CFT method estimations. Therefore, it is more likely that this fluctuation is due to an environmental factor that is not clear to the authors.

With respect to significant wave height, ocean wave spectra estimates generated using both methods were used to estimate the significant wave height via the Signal to Noise Ratio (SNR) method outlined in [3] and [18]. Figure 19 shows the significant wave height estimates generated using the CFT-without-ISAF and CFT-with-ISAF methods. The parameters c_0 and c_1 are the calibration coefficients acquired using the radar training process as described in [3]. The mean absolute error in significant wave height estimation, $\overline{|\varepsilon_{Hs}|}$, was calculated for both methods. As listed in Table 3, estimation errors, $\overline{|\varepsilon_{Hs}|}$, of 0.57 m and 0.54 m were obtained using the CFT-without-ISAF and CFT-with-ISAF, respectively. Even though the CFT-with-ISAF method produces more accurate estimates for ocean wave spectra, similar estimation performance for significant wave height was achieved using the CFT-without-ISAF and the CFT-with-ISAF, with a slight advantage for the CFT-with-ISAF method. This may be due to the fact that both methods were calibrated against ground truth data. Therefore, different calibration coefficients, c_0 and c_1, were obtained for each method and annotated in Figure 19.

IV. CONCLUSIONS AND FUTURE WORK

In the literature, the process of ocean surface sampling using X-band marine radar has been considered as a standard point sampling. The influence of ocean surface sampling on the ocean wave spectra estimation using the CFT has not been previously addressed. In this paper, the ocean surface sampling process by a marine radar has been reviewed and investigated as an averaging process. A 2D low pass filter model has been presented to describe the effect of the sampling process on the CFT method estimates of ocean wave spectra. Furthermore, a filter referred to as the Inverse Sampling Moving Average Filter (ISAF) has been proposed to mitigate that effect. The performance of the ISAF was validated on field radar data against ground truth data that were obtained from a TRIAXYS Wave Rider buoy. Results show that implementing the ISAF in the CFT method of ocean wave spectral estimation improves the accuracy of the method. The improvement measures that were considered in this paper include the accuracy of estimating the non-directional wave spectrum, and the accuracy of derived parameter estimates, including, the peak wave period, the mean wave period, the zero-crossing wave period, and the peak wave direction. The ISAF performance was also validated in terms of significant wave height estimation and it was found that the ISAF method and the standard

CFT method produced comparable results. Future work on the ISAF will include further validation involving other ocean state parameters such as surface current information.

ACKNOWLEDGMENT

The radar field data and ground truth buoy data are provided by Defence Research and Development Canada (DRDC).

REFERENCES

[1] I. Young, W. Rosenthal, and F. Ziemer, "A three-dimensional analysis of marine radar images for the determination of ocean wave directionality and surface currents," *J. Geophys. Res.*, vol. 90, no. C1, pp. 1049–1059, 1985.
[2] J. C. Nieto-Borge, "Inversion of marine radar images for surface wave analysis," *J. Atmos. Ocean. Technol.*, vol. 31, pp. 1059–1291, Aug. 2004.
[3] J. C. Nieto-Borge, K. Hessner, P. Jarabo-Amores, and D. De La Mata-Moya, "Signal-to-noise ratio analysis to estimate ocean wave heights from X-band marine radar image time series," *IET Radar Sonar Navigat.*, vol. 2, no. 1, pp. 35–41, Feb. 2008.
[4] P. H. Y. Lee *et al.*, "X band microwave backscattering from ocean waves," *J. Geophys. Res., Oceans*, vol. 100, no. C2, pp. 2591–2611, 1995.
[5] W. J. Plant and W. C. Keller, "Evidence of Bragg scattering in microwave doppler spectra of sea return," *J. Geophys. Res., Oceans*, vol. 95, no. C9, pp. 16299–16310, 1990.
[6] B. Lund, C. Collins, H. Graber, E. Terrill, and T. Herbers, "Marine radar ocean wave retrieval's dependency on range and Azimuth," *Ocean Dyn.*, vol. 64, no. 7, pp. 999–1018, 2014.
[7] A.-A. Al-Habashneh, C. Moloney, E. W. Gill, and W. Huang, "An adaptive method of wave spectrum estimation using X-band nautical radar," *Remote Sens.*, vol. 7, no. 12, p. 15851, 2015. [Online]. Available: http://www.mdpi.com/2072-4292/7/12/15851
[8] Z. Chen, B. Zhang, Y. He, Z. Qiu, and W. Perrie, "A new modulation transfer function for ocean wave spectra retrieval from X-band marine radar imagery," *Chin. J. Oceanol. Limnol.*, vol. 33, no. 5, pp. 1132–1141, 2015.
[9] G. Ludeno, F. Raffa, F. Soldovieri, and F. Serafino, "X-band radar for the monitoring of sea waves and currents: A comparison between medium and short radar pulses," *Geosci. Instrum., Methods Data Syst. Discussions*, vol. 2017, pp. 1–11, Jan. 2017. [Online]. Available: https://www.geosci-instrum-method-data-syst-discuss.net/gi-2016-42/gi-2016-42.bib
[10] M. Skolnik, *Radar Handbook*, 3rd ed. New York, NY, USA: McGraw-Hill, 2008.
[11] B. Edde, *Radar Principles, Technology, Applications*. Englewood Cliffs, NJ, USA: Prentice-Hall, 1995.
[12] D. H. Nomiyama and T. Hirayama, "Evaluation of marine radar as an ocean-wave-field detector through full numerical simulation," *J. Marine Sci. Technol.*, vol. 8, no. 2, pp. 88–98, 2003.
[13] M. Farmer and S. Sohn, "Programmed radar coordinate scan conversion," U.S. Patent 55 194 010 521, May 21, 1996.
[14] U. Graf, *Applied Laplace Transforms and Z-Transforms for Scientists and Engineers*. Basel, Switzerland: Birkhäuser Verlag, 2004.
[15] K. Nickerson and S. Haykin, "Scan conversion of radar images," *IEEE Trans. Aerosp. Electron. Syst.*, vol. 25, no. 2, pp. 166–175, Mar. 1989.
[16] *The Wave and Surface Current Monitoring System (WaMoS) II Operating Manual*, 4th ed., OceanWaves GmbH, Luneburg, Germany, May 2012.
[17] M. Tucker, *Waves in Ocean Engineering: Measurement, Analysis, Interpretation*. New York, NY, USA: Ellis Horwood, 1991.
[18] H. Dankert, J. Horstmann, and W. Rosenthal, "Wind- and wave-field measurements using marine X-band radar-image sequences," *IEEE J. Ocean. Eng.*, vol. 30, no. 3, pp. 534–542, Jul. 2005.

AL-ABBASS AL-HABASHNEH (S'08) received the B.Sc. degree (Hons.) in electrical engineering from Mutah University, Al-Karak, Jordan, in 2002, and the master's and Ph.D. degrees in electrical engineering from the Memorial University of Newfoundland, St. Johns, NL, Canada, in 2010 and 2017, respectively. His research interests include ocean wave spectra and sea state parameter estimation from *X*-band marine radar data.

CECILIA MOLONEY (M'91) received the B.Sc. degree (Hons.) in mathematics from the Memorial University of Newfoundland, St. Johns, NL, Canada, in 1978, and the M.A.Sc. and Ph.D. degrees in systems design engineering from the University of Waterloo, Waterloo, ON, Canada, in 1980 and 1988, respectively. Since 1990, she has been a Faculty Member with the Memorial University of Newfoundland, where she is currently a Full Professor of electrical and computer engineering. Her research interests include nonlinear signal- and image-processing methods, signal representations via wavelet and contourlet transforms, radar signal processing, transformative pedagogy for science and engineering, and gender and science studies. From 2004 to 2009, she held the NSERC/Petro-Canada Chair for Women in Science and Engineering, Atlantic Region.

ERIC W. GILL (M'00–SM'05) received the B.Sc. degree in physics and the M.Eng. and Ph.D. degrees in electrical engineering from the Memorial University of Newfoundland, St. Johns, NL, Canada, in 1977, 1990, and 1999, respectively. In 1977, he was a Lecturer in physics with the College of the North Atlantic (formerly, Cabot Institute of Applied Arts and Technology), St. Johns, NL. Since 2000, he has been with the Faculty of Engineering and Applied Science, Memorial University of Newfoundland, where he is currently a Professor, carrying out teaching and research in theoretical and applied electromagnetics. His research interests include the scattering of high-frequency electromagnetic radiation from time-varying, randomly rough surfaces, with particular application to the use of ground wave radar in remote sensing of the marine environment. He is a member of the American Geophysical Union.

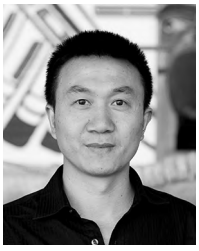

WEIMIN HUANG (M'10–SM'13) received the B.S., M.S., and Ph.D. degrees in radio physics from Wuhan University, Wuhan, China, in 1995, 1997, and 2001, respectively, and the M.Eng. degree in engineering electromagnetics from the Memorial University of Newfoundland, St. John's, NL, Canada. He received the Post-Doctoral Fellowship from Memorial University of Newfoundland.

From 2008 to 2010, he was a Design Engineer with Rutter Technologies, St. John's, NL. Since 2010, he has been with the Faculty of Engineering and Applied Science, Memorial University of Newfoundland, where he is currently an Associate Professor. He has authored over 170 research papers. His current research interests include the mapping of oceanic surface parameters via high-frequency ground wave radar, *X*-band marine radar, and global navigation satellite systems.

Dr. Huang has been a Technical Program Committee Member. He served as a Technical Program Co-Chair of the IEEE Newfoundland Electrical and Computer Engineering Conference in 2012 and 2013. He serves as a regular Reviewer over 40 international journals and a Reviewer for many IEEE international conferences, such as RadarCon, ICC, GLOBECOM, IGARSS, and Oceans. He has been the Lead Guest Editor of the Special Issue on Advances in Coastal HF and Microwave (*S*- or *X*-band) Radars of the *International Journal of Antennas and Propagation*. He is an Associate Editor of the IEEE Access and an Editorial Board Member of *Remote Sensing*.